AGU PUBLICATIONS

Geochemistry, Geophysics, Geosystems

RESEARCH ARTICLE
10.1002/2014GC005661

Viscosity measurements of crystallizing andesite from Tungurahua volcano (Ecuador)

Magdalena Oryaëlle Chevrel[1,2], Corrado Cimarelli[2], Lea deBiasi[2,3], Jonathan B. Hanson[4], Yan Lavallée[5], Fabio Arzilli[6], and Donald B. Dingwell[2]

[1]Instituto de Geofísica, Departamento de Vulcanología, Universidad Nacional Autónoma de México, México D.F, Mexico, [2]Department of Earth and Environmental Sciences, Ludwig-Maximilians-Universität, Munich, Germany, [3]Karlsruhe Institute of Technology, Institute of Applied Materials, Eggenstein-Leopoldshafen, Germany, [4]Department of Earth Sciences, University of Bristol, Bristol, UK, [5]Department of Earth, Ocean and Ecological Sciences, University of Liverpool, Liverpool, UK, [6]Instituto Nazionale di Geofisica e Vulcanologia, Sezione di Pisa, Pisa, Italy

Abstract Viscosity has been determined during isothermal crystallization of an andesite from Tungurahua volcano (Ecuador). Viscosity was continuously recorded using the concentric cylinder method and employing a Pt-sheathed alumina spindle at 1 bar and from 1400°C to subliquidus temperatures to track rheological changes during crystallization. The disposable spindle was not extracted from the sample but rather left in the sample during quenching thus preserving an undisturbed textural configuration of the crystals. The inspection of products quenched during the crystallization process reveals evidence for heterogeneous crystal nucleation at the spindle and near the crucible wall, as well as crystal alignment in the flow field. At the end of the crystallization, defined when viscosity is constant, plagioclase is homogeneously distributed throughout the crucible (with the single exception of experiment performed at the lowest temperature). In this experiments, the crystallization kinetics appear to be strongly affected by the stirring conditions of the viscosity determinations. A TTT (Time-Temperature-Transformation) diagram illustrating the crystallization "nose" for this andesite under stirring conditions and at ambient pressure has been constructed. We further note that at a given crystal content and distribution, the high aspect ratio of the acicular plagioclase yields a shear-thinning rheology at crystal contents as low as 13 vol %, and that the relative viscosity is higher than predicted from existing viscosity models. These viscosity experiments hold the potential for delivering insights into the relative influences of the cooling path, undercooling, and deformation on crystallization kinetics and resultant crystal morphologies, as well as their impact on magmatic viscosity.

Key Points:
- Viscosity determination at subliquidus temperatures of an andesitic sample
- Use of disposable Pt-sheathed alumina spindles
- Description of viscosity and crystallization kinetics under constant stirring

Supporting Information:
- Supporting Information

Correspondence to:
M. O. Chevrel,
oryaelle.chevrel@gmail.com

Citation:
Chevrel, M. O., C. Cimarelli, L. deBiasi, J. B. Hanson, Y. Lavallée, F. Arzilli, and D. B. Dingwell (2015), Viscosity measurements of crystallizing andesite from Tungurahua volcano (Ecuador), *Geochem. Geophys. Geosyst.*, *16*, 870–889, doi:10.1002/2014GC005661.

Received 14 NOV 2014
Accepted 10 FEB 2015
Accepted article online 19 FEB 2015
Published online 25 MAR 2015

1. Introduction

The viscosity of magma governs its transport at all scales during the geological evolution of a planet. It controls the emplacement rate and flow behavior of any magmatic body. Silicate liquids are Newtonian fluids over a wide range of long time scales [*Dingwell and Webb*, 1989; *Webb and Dingwell*, 1990] and the description of the liquid viscosity-temperature-composition relationships in that regime has received much attention in the last decade [e.g., *Giordano et al*., 2008; *Hui and Zhang*, 2007]. The viscosity, however, may change significantly when gas bubbles and crystals nucleate and grow, henceforth partitioning strain and modifying the resultant rheology. Many experimental studies have attempted to formulate a tractable and robust rheological description of magmas bearing (1) crystals [e.g., *Ryerson et al*., 1988; *Pinkerton and Stevenson*, 1992; *Lejeune and Richet*, 1995; *Pinkerton and Norton*, 1995; *Saar et al*., 2001; *Sato*, 2005; *Ishibashi and Sato*, 2007; *Caricchi et al*., 2007; *Costa*, 2005; *Costa et al*., 2009; *Petford*, 2009; *Ishibashi*, 2009; *Mueller et al*., 2010; *Castruccio et al*., 2010; *Vona et al*., 2011; *Cimarelli et al*., 2011], (2) bubbles [*Bagdassarov and Dingwell*, 1992; *Lejeune et al*., 1999; *Stein and Spera*, 2002; *Manga et al*., 1998; *Saar and Manga*, 1999], and (3) both crystals and bubbles [e.g., *Bagdassarov et al*., 1994; *Stein and Spera*, 1992; *Lavallée et al*., 2007, 2012; *Harris and Allen*, 2008; *Pistone et al*., 2012; *Avard and Whittington*, 2012]. It has been experimentally demonstrated that the apparent viscosity of an analog suspension (containing solid particles in a Newtonian liquid) increases nonlinearly with particle fraction and, if particle interaction takes place, then the rheology becomes non-Newtonian, exhibiting strain-rate dependence [*Mader et al*., 2013]. At higher crystallinity, the viscosity of

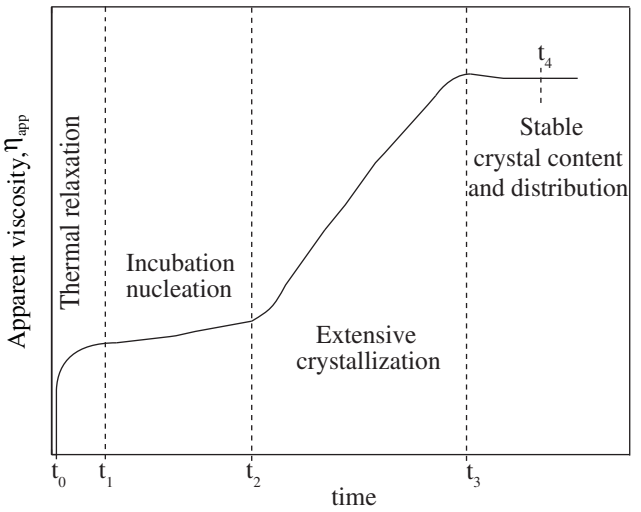

Figure 1. Schematic viscosity-time path at subliquidus temperature (from *Vona and Romano*. [2013]).

magma increases sharply as the particle content approaches a maximum crystal packing value, which is strongly dependent on the particle shape and size distribution. Beyond this transition, magma exhibits pseudoplastic rheology [e.g., *Lavallée et al*., 2007].

The viscosity of a suspension may be measured by various methods. Some studies on analog materials have employed flow morphology characteristics [e.g., *Castruccio et al*., 2010] and several have involved viscosity measurements using parallel-plate rheometers [*Mueller et al*., 2010; *Cimarelli et al*., 2011; *Del Gaudio et al*., 2013]. For magmatic suspensions, the viscosity at low temperature (800–900°C), and thus in a highly viscous liquid, has been measured at 1 bar using uniaxial presses [e.g., *Lejeune and Richet*, 1995; *Bouhifd et al*., 2004; *Villeneuve et al*., 2008; *Lavallée et al*., 2007; *Cordonnier et al*., 2009, and references within] and at high pressure in torsion in Patterson presses [e.g., *Caricchi et al*., 2007; *Pistone et al*., 2012, and references therein].

At higher subliquidus temperatures (1100–1200°C) and thus in less viscous melts, rotational viscometry (concentric cylinder) has typically been employed. An early investigation of this kind was undertaken by *Shaw* [1969], who remelted basalt (sampled from a lava flow), and measured its viscosity during cooling below the liquidus. Later, *Ryerson et al*. [1988] and *Pinkerton and Norton* [1995] made use of the same method to expand the data set of crystallizing basaltic lava viscosity. In these pioneering studies, the tested lava was not sampled during crystallization, instead crystal content was estimated independently using the liquid line-of-descent provided by petrological thermodynamic models. In order to extract petrological information on the rheological effects of crystals on magmas, *Sato* [2005] allowed a basaltic liquid to crystallize then inserted a spindle to measure the viscosity as well as to sample the melt; these steps were repeated at successively lower temperature states. The sampled product was then used to estimate the crystal fraction. This method has been further applied by *Ishibashi and Sato* [2007] and *Ishibashi* [2009] to expand the rheological description of crystallizing basaltic magmas. Although these tests are very informative, the method has shortcomings: first, there was no continuous recording (only punctual reading) of the viscosity progression during cooling and crystallization and thus, no confirmation of the achievement of thermodynamic equilibrium; second, by dipping/extracting the spindle, the sample and (more importantly) the crystalline textures are disturbed; third, the investigation of the crystal fraction is limited to the portion of melt agglutinated to the spindle, thus not being representative of the whole sample; and fourth, they used an alumina spindle directly exposed to the melt that is, strictly speaking, only suitable for Al_2O_3-saturated material otherwise reaction with the melt cannot be excluded.

In order to overcome such disadvantages, *Vona et al*. [2011] and *Vona and Romano* [2013] chose to record continuously the viscosity changes during cooling and crystallization, and thus monitor the rheological consequences of the crystallization of the suspension. The viscosity-time paths obtained through crystallization have been divided into four stages. The first stage (from t_0 to t_1, Figure 1) corresponds to the near-instantaneous viscosity increase with decreasing temperature, which is attributed to the thermal relaxation of the melt at the dwell temperature (equilibrium melt viscosity). The second stage (from t_1 to t_2) is a near constant viscosity-time path associated with "the nucleation incubation time" defines as the time required before rheologically perceptible crystallization takes place. The onset of the third stage (at t_2) is marked by a sharp viscosity increase attributed to extensive crystallization (although t_2 does not define the exact onset of crystallization which is likely to have initiated in a rheologically imperceptible way at an earlier stage. The

Table 1. Bulk Rock Composition of Tungurahua's Andesite

Oxide	wt %	Normalized wt %
SiO_2	56.31	57.49
Al_2O_3	16.41	16.75
Fe_2O_3T[a]	7.37	7.52
MnO	0.12	0.12
MgO	4.66	4.76
CaO	6.59	6.73
Na_2O	3.96	4.04
K_2O	1.41	1.44
TiO_2	0.89	0.91
P_2O_5	0.24	0.25
LOI	−0.20	
Total	97.96	100

[a] Fe_2O_3T = total iron as Fe_2O_3.

fourth and last stage (from t_3 to t_4) is reached when viscosity becomes time-invariant and is associated with stable crystal content and distribution (and therefore thermodynamic equilibrium) and with the alignment of crystals in the flow field. *Vona et al*. [2011] used a massive $Pt_{80}Rh_{20}$ spindle (to avoid contamination) and thus had to remove it before quenching and dissection of the final product. While this technique allows the textural analysis of a larger sample volume, as noted above, distortion of the original textures during spindle removal cannot be entirely excluded.

In this study, we adapt this method by using an alumina spindle sheathed in a thin-walled platinum tube which we leave in the sample during quenching, thereby preserving all original attributes of the crystalline phase distribution and orientation produced during the viscosity measurement at each temperature increment. In this way, we can test the reproducibility of the method and better constrain the characteristics of the crystalline phase across the complete viscosity-time path. Here this technique is used to measure the crystallization-dependence of the viscosity of remelted andesitic lava. We present both the melt viscosity above the liquidus and the viscosity of equilibrated crystal-bearing suspensions for various subliquidus temperatures as a function of crystal volume fraction, interstitial melt composition, and strain-rate.

2. Experimental Method

2.1. Starting Material

The andesite sample used here was erupted during the 2006 Plinian activity of Tungurahua, Ecuador; and was collected from the dense pyroclastic flow as described in *Douillet et al*., [2013]. The bulk rock chemistry has been determined by X-ray fluorescence spectrometry (XRF) using a Phillips MigiXPRO at LMU (Table 1). The rock sample is dense, with a porosity of only 1%. Petrographic observations reveal a seriate porphyritic texture containing 20 vol % of tabular plagioclase with a size range from microlites up to 1 mm as well as 15 vol % of pyroxenes, showing a similar size distribution, both in a hypocrystalline groundmass.

For each experiment, a separate piece of a single block was crushed, melted in a box furnace for 2 h at 1400°C, homogenized by stirring and quenched; this was repeated multiple times to ensure homogeneity.

2.2. Experimental Setup

The viscosity was measured via the concentric cylinder method using a Brookfield DV-III+ viscometer head (full scale torque of 7.2×10^{-4} Nm), similar to the one detailed in *Dingwell* [1986] and used by *Vona et al*. [2011]. The viscometer head drives the spindle at constant speed and digitally records the torque exerted on the spindle by the sample. The angular velocities used ranged from 0.01 to 40 rotations per minute (RPM) and correspond to mean strain rates from 0.002 to 8.5 s^{-1}. The crucible containing the lava and the rotating spindle has diameters of 26 mm and 3 mm, respectively. The ratio of inner to outer radius of the two cylinders ($R_i/R_o = 0.12$) corresponds to a "wide-gap geometry" where the shear stress is inversely proportional to the distance from the spindle toward the outer cylinder [*Landau and Lifshitz*, 1987].

2.3. Adapted Spindle Design

In previous studies, viscosity measurements at subliquidus conditions were performed with a spindle made either of massive $Pt_{80}Rh_{20}$ [*Vona et al*., 2011] or aluminum oxide [*Sato*, 2005; *Ishibashi*, 2009]. In both studies, the spindle was extracted from the material prior to cooling and the texture of the sample was thereby compromised. Here we treated our spindles as disposable parts that have been left in the suspension during the whole experiment and quenching process in order to examine the distribution and alignment of the crystals from the spindle to the crucible wall. In this manner, any disturbance of the sample due to spindle extraction has been avoided.

The disposable spindle is made of Al_2O_3 (AL23) ceramic rod (330 mm in length, 3 mm in diameter) and the end that is immersed in the melt is tightly sheathed with a platinum tube (0.02 mm wall thickness and

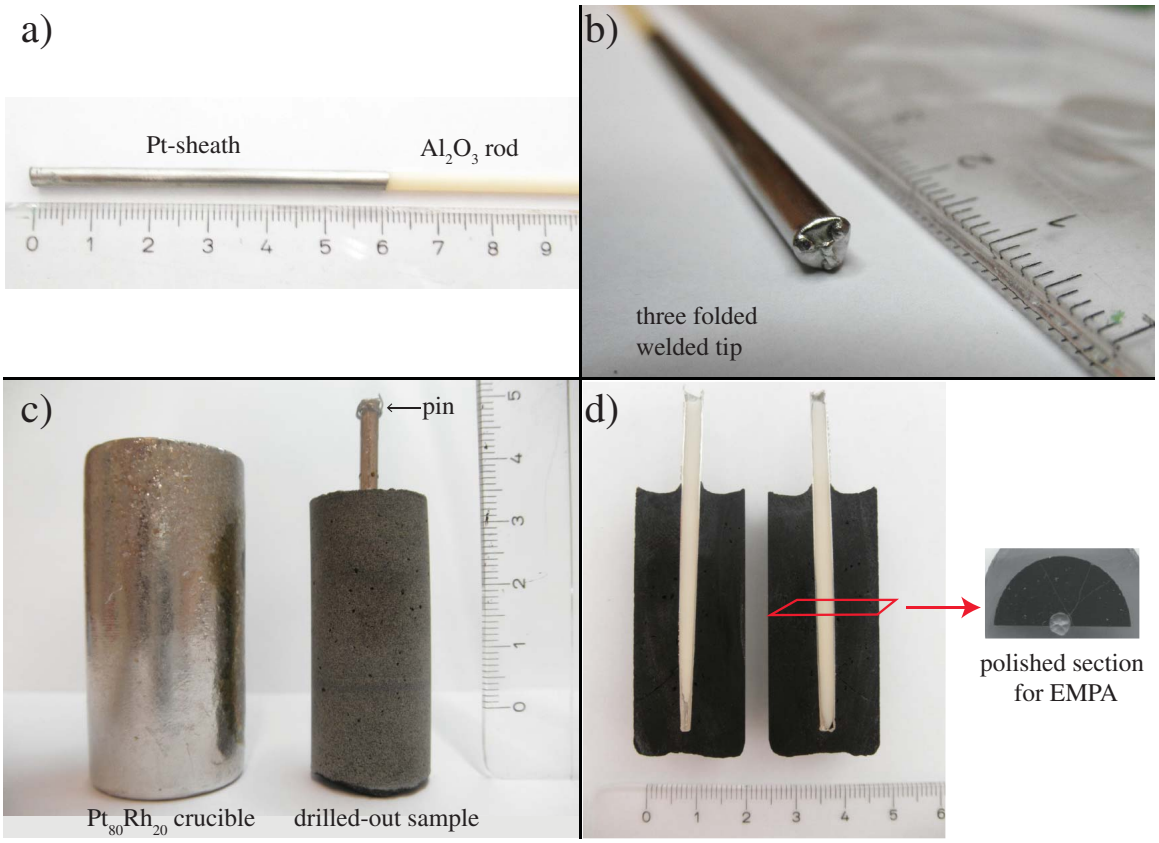

Figure 2. Disposable spindle. (a) Al_2O_3 ceramic rod sheathed by a Pt-tube; (b) tip of the Pt-sheath tri-welded into a symmetrical star shape; (c) Pt_{80}-Rh_{20} crucible and drilled-out final product with the spindle sticking out of the sample, the top of the spindle reveals the pin used to attach the Pt-sheath to the alumina rod; and (d) photographs of the final experimental product cut along length and further sectioned radially for EMP analyses.

55 mm long). The Pt-sheath is fixed to the Al_2O_3 ceramic rod via a horizontal Pt-pin passing through the tube and the rod in order to avoid any slip between the Pt-sheath and the alumina rod. In order to minimize any end effects of the spindle geometry the tip of the Pt-sheath was triwelded into a symmetrical star shape (Figure 2). One advantage of the Pt-sheath is its long-term inertness that prevents any high-temperature reaction between alumina spindle, Pt-sheath and the sample. One potential disadvantage is the slight variation in geometry from one fabricated spindle sheath to the next. Therefore, every spindle assembly used here was calibrated using a viscosity standard melt, DGG-1, for which the temperature-viscosity relationship is well known. The relationship between torque and viscosity was established for the strain-rate range of the experiments and was used to calibrate all viscosity determinations made with that spindle. The precision of the viscosity determinations is estimated at $\pm 3\%$ (2σ) [*Dingwell*, 1986]. After calibration, the Pt-sheath of the spindle was cleaned in HF and reused for measurement of the natural melt.

At the termination of each experiment, the spindle was simply detached (taking care to minimize any absolute displacement) from the viscometer head and the crucible was removed from the bottom of the furnace to quench the suspension with the spindle still intact and fully immersed (Figure 2). For this rapid operation, the quenching rate is estimated to be a few degrees per second, which, for these samples, prevents significant further nucleation and growth of crystals. The spindle was severed just above the crucible edge and the inner 22 mm of the solidified material was cored out from the crucible using a diamond corer. This operation inevitably leaves ca. 1 mm of material attached to the crucible. The cores were sectioned parallel and perpendicular to the spindle. The exact immersion depth of the spindle is determined optically at this point. For each sample, a section of a half cylinder perpendicular to the spindle was taken from the middle of the crucible and was polished and coated for further microprobe analysis (Figure 2). The crucible is cleaned in HF and used again for the next experiment using new material and a new, calibrated, disposable spindle.

Table 2. Notation of All Variables

Variable	Unit	Definition
T_{exp}	°C	Temperature of the experiment
$T_{liquidus}$	°C	Liquidus temperature estimated with MELTS
ΔT		Undercooling ($=T_{liquidus} - T_{exp}$)
T	S	Time (see Figure 1)
Ω	rad/s	Angular velocity
$\dot{\gamma}$	s^{-1}	Strain-rate calculated from equation (1)
M	N m	Torque fraction (full torque for this instrument is 7.4×10^{-4} N m)
R_o	M	Radius of the outer cylinder (crucible)
R_i	M	Radius of the inner cylinder (spindle)
h	M	Spindle immersion depth
σ	Pa	Stress calculated from equation (3)
η_{app}	Pa s	Measured aparent viscosity
η_{melt}	Pa s	Viscosity of the interstitial melt calculated from its chemical composition using *Giordano et al.* [2008]
η_r		Relative vicosity ($=\eta_{app}/\eta_{melt}$)
K_r		Relative consistency
K	Pa s	Consistency
n		Flow index
ϕ		Crystal fraction area calculated from binary images using the software ImageJ in the area marked in Figure 7
R		Aspect ratio of plagioclase using the ten biggest crystals
ϕ_{max}		Maximum packing calculated using *Mueller et al.* [2010] $= 2/(0.321\ R + 3.02)$
L	mm	Average length of the plagioclase long axis
A_r	mm^2	Cross-sectional area
I_r	$1/m^3s$	Nucleation rate calculated from equation (4)
G_r	m/s	Growth rate calculated from equation (7)
N_v	$1/mm^3$	Volumetric number density calculated from equation (5)
s_n	mm	Mean crystal size calculated from equation (6)
N_a	$crystal/mm^2$	Crystal number density estimated from BSE images

2.4. Viscosity Measurements

During the viscosity measurements, the torque, the angular velocity, and the furnace temperature are continuously monitored at 1 Hz and the viscosity data are displayed as a function of time. The melt initially at a superliquidus temperature of 1400°C was first stirred at 40 RPM for 300 min. The temperature was subsequently dropped to a subliquidus temperature (T_{exp}) at the maximum cooling rate sustainable by the furnace (~0.15°C/s) with continuous stirring of the sample. During the cooling, and subsequent crystallization, the viscosity increases and the rotational velocity of the rotating spindle is automatically halved when the maximum instrument torque is reached.

The apparent viscosity of the suspension is defined as the ratio of the stress (σ) over strain-rate ($\dot{\gamma}$) and calculated using geometrical dimensions as follows (all variables are given in Table 2). The strain-rate is estimated from the applied angular velocity:

$$\dot{\gamma} = \frac{2\Omega}{n\left(1-\frac{R_0}{R_i}\right)^{2/n}} \quad (1)$$

The stress is the resistance of the material to flow:

$$\sigma = \frac{M}{2\pi h R_i^2} \quad (2)$$

To describe the non-Newtonian rheology of the two-phase suspension the consistency (K) and the flow index (n) are calculated according to the *Herschel and Bulkley* [1926] equation:

$$\sigma = K\dot{\gamma}^n \quad (3)$$

where the consistency is the viscosity for Newtonian flow when $n = 1$.

2.5. Experimental Conditions

This study comprises three sets of data. One set is the viscosity of the pure melt that was first measured in 50°C steps of decreasing temperature from 1395°C down to 1098°C. For each step, the temperature was

held constant until the liquid had thermally relaxed and a stable torque was recorded, before the onset of any crystallization.

The second set is a suite of time domain experiments comprising four isothermal runs at a subliquidus temperature of 1162°C, but quenched in at different stages of the crystallization process in order to examine the crystallization kinetics and the associated suspension viscosity. Run 1 was stopped during the incubation time, run 2 during the "crystallization slope" and runs 3 and 4 when stable viscosity readings were achieved, corresponding to completed runs with stable crystal contents.

The third set of data corresponds to "completed" runs (where crystallization reached equilibrium) at various subliquidus isotherms: T_{exp} = 1180, 1168, 1157, 1152, 1144°C. Lower subliquidus temperatures could not be completed as extensive crystallization resulted in viscosities exceeding the instrumental limits (torques corresponding to viscosity above 10^5 Pa s). The durations of the experiments lie between 93 and 257 h, depending on T_{exp}.

2.6. Chemical Analyses of the Experimental Products

Chemical compositions of the experimental products (glass and crystals) were investigated using a Cameca SX100 electron probe microanalyzer (EPMA) at LMU. Polished sections were coated with carbon and analyzed with a focused beam (for crystals) and with a defocused beam of 10 μm (for glass) operating at 15 kV acceleration voltage and 5 nA sample current in order to minimize alkali loss. Standards used are: Wollastonite (Si, Ca), Corundum (Al), Ilmenite (Ti, Mn), Hematite (Fe), Albite (Na), Apatite (P), Periclase (Mg), and Orthoclase (K). All reported glass and crystal compositions are averages of a minimum of 10–15 analyses. Glass data were collected from microlite-free regions. Each measurement point was selected using back-scattered electron imaging and reflected light microscopy to ensure good surface quality and focusing.

2.7. Texture Analyses, Nucleation Rate, and Crystal Growth

Back-scattered electron (BSE) images were automatically collected using the same EPMA Cameca SX100. The BSE images of selected representative areas were filtered through various thresholds using the software ImageJ to produce binary images of crystals and melts for further analysis. We further used the software to measure the crystal fraction (ϕ). Using the software JMicrovision, each crystal was manually picked and we analyzed the crystal number density, the average length of the long axis of the plagioclases (L) and the deviation angle of the plagioclase long axis to the tangent of the theoretical circular flow line imposed by the stirring.

The average nucleation rate (I_r) and the maximum crystal growth rate (G_r) of plagioclase were calculated using the relationship given by *Couch et al.* [2003]:

$$I_r = \frac{N_v}{t_3 - t_1} \tag{4}$$

where t_1 is the time when melt relaxation is reached and marks the start of the incubation time and t_3 corresponds to the end of extensive crystallization, when viscosity becomes constant through time and hence when thermodynamic equilibrium is reached; the volumetric number density (N_v) is calculated using:

$$N_v = \frac{N_a}{S_n} \tag{5}$$

which requires knowledge of the crystal number density (N_a) obtained from analysis of BSE images and the mean crystal size (s_n) of the plagioclase obtained with:

$$s_n = \left(\frac{\phi}{N_a}\right)^{1/2} \tag{6}$$

The maximum crystal growth rate (G_r) can be calculated using:

$$G_r = 0.5\frac{L}{(t_3 - t_1)} \tag{7}$$

(Note: all variables are presented in Table 2.)

Table 3. Viscosity of Tungurahua's Andesitic Melt Experimentally Measured and Calculated Using *Giordano et al.* [2008]

T (°C)	log η (Pa s) This Study	log η (Pa s) *Giordano et al.* [2008]
1395	1.63	1.62
1345	1.93	1.90
1296	2.21	2.21
1246	2.51	2.55
1197	2.86	2.92
1098	3.70	3.80

3. Results

3.1. Viscosity of the Initial Melt

The viscosity of the initial melt is given in Table 3. Although the liquidus temperature ($T_{liquidus}$) was estimated at 1180°C using MELTS (which is based on static experiments) [*Ghiorso and Sack*, 1995] at atmospheric pressure and ambient oxygen fugacity, we were also able to measure the viscosity of the pure melt in its metastable state at 1098°C (the viscosity was recorded as soon as the melt was fully thermally relaxed and before crystallization started). The viscosity of the pure melt could not be measured below this temperature as the time before crystallization becomes too short to allow a measurement. The calculated viscosity using the GRD model [*Giordano et al.*, 2008] is in very good agreement with our experimental data (Table 3).

3.2. Time Domain Experiments: Crystallization Kinetics and Suspension Viscosity

The viscosity-time path of the repeated experiments at 1162°C is shown in Figure 3 and reported in Tables 4 and 5 (together with the proportions and characteristics of the phases encountered).

3.2.1. Incubation Time

Run 1 was stopped during the incubation time before the large viscosity increase. Although the exact onset of nucleation could not be ascertained simply from the viscosity-time path using our experimental protocol (as the first nuclei would not lead to a significant viscosity increase), we consider the incubation time to approximate $t_2 - t_1$, which for run 1 reached 54 h. In contrast, the other runs exhibit shorter incubation times, down to as little as 6 h for run 4. A slight, 7×10^{-4} to 1.4×10^{-3} log Pa s/h viscosity increase was measured during incubation.

BSE images of run 1 (not shown here) reveal a near-aphyric texture (small irregularities in the image *may* be due to the presence of unidentified nanocrystals). The chemical composition of the quenched glass differs slightly from the original material (see supporting information): it is enriched in SiO_2 (+0.9 wt %) and depleted in Na_2O (−0.7 wt %).

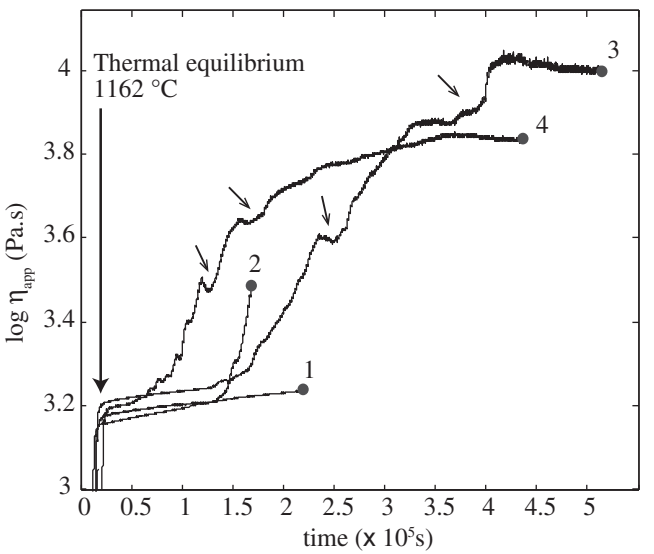

Figure 3. Viscosity measurements of the repeated experiments at 1162°C and quenched at different stages of the process (gray spots): run 1 was stopped during the incubation time before extensive crystallization, run 2 was stopped in the middle of the viscosity increase due to extensive crystallization, and runs 3 and 4 were both stopped at isoviscous behavior, in the stable crystal content and distribution field. Small arrows indicate irregularities in the viscosity measurements.

3.2.2. Extensive Crystallization

Run 2 was stopped during the large viscosity increase attributed to extensive crystallization (between t_2 and t_3). Here viscosity increased at a rate of 2.8×10^{-2} log Pa s/h. This contrasts with run 3 and 4, which showed viscosity-time path of 9.9×10^{-3} and 7.5×10^{-3} log Pa s/h, respectively. We note that the sharp viscosity increase is occasionally accompanied by brief subordinate oscillation in viscosity (<0.05 log Pa s), which can last up to a few hours until viscosity increases again (small arrows in Figure 3). The BSE image of run 2 shows two areas of plagioclase-bearing melt, a central one along the spindle and a distal one along the crucible wall, separated by a 4 mm thick crystal-free melt ring (Figure 4). The central area near the spindle is divided

Table 4. Experimental Results of Viscosity (η), Temperature (T), and Time (t) of Each Isothermal Measurements

T_{exp} (°C)	1180	1168	1162 run 1	1162 run 2	1162 run 3	1162 run 4	1157	1152	1144
ΔT (°C)	0	12	18	18	18	18	23	28	36
t_1 (s)	2.8E+04	2.7E+04	2.5E+04	2.7E+04	3.0E+04	3.1E+04	2.4E+04	2.3E+04	2.3E+04
log $\eta(t_1)$ (Pa s)	2.98	3.18	3.16	3.18	3.21	3.20	3.16	3.15	3.23
t_2 (s)	4.6E+05	9.2E+04	2.2E+05[a]	1.3E+05	1.3E+05	5.2E+04	2.7E+05	4.0E+05	6.8E+04
log $\eta(t_2)$ (Pa s)	3.09	3.20	3.23[a]	3.21	3.24	3.20	3.24	3.21	3.26
t_3 (s)	8.9E+05	4.8E+05		1.7E+05[a]	4.2E+05	3.6E+05	4.3E+05	5.5E+05	2.9E+05
log $\eta(t_3)$ (Pa s)	3.57	3.75		3.49[a]	4.03	3.85	3.95	4.07	4.85
t_4 (s)	9.5E+05	5.0E+05			5.1E+05	4.3E+05	5.9E+05	6.1E+05	3.6E+05
log $\eta(t_4)$ (Pa s)[b]	3.59	3.77			4.05	3.86	3.93	4.11	4.80

[a]Values when the experiments were stopped.
[b]Apparent viscosity at strain-rate indicated in Table 5.

into two zones. The area within the first 1 mm of the spindle contains a population of plagioclase ($N_a = 164$ crystals/mm^2) with length/width ratio dominantly around 7 (average length of 0.1 mm). The next 2 mm of the area is composed of a higher density of crystals ($N_a = 365$ crystals/mm^2) with length/width ratio dominantly around 10 (average length of 0.08 mm). This central crystal-bearing area ends with an abrupt crystal front against a crystal-free glass. The plagioclase-bearing area near the crucible is more dispersed ($N_a = 100$ crystals/mm^2) but the plagioclase crystals are longer (up to 0.5 mm). A wide range of deviation angle of the crystals' long axis from the theoretical flow line, indicative of a poor crystal alignment for the crystals is observed near the wall while near the spindle the crystals are more aligned with the flow lines (see supporting information). This observation agrees well with the relative proportions of crystals in the two areas, i.e., the opportunity of crystals to freely rotate as well as the gradient in shear stress expected in this geometry.

Chemical analyses along a profile from spindle to crucible wall (see supporting information) reveal different degrees of interstitial melt fractionation in crystal-bearing areas and in the crystal-free gap. We observed a significant depletion in Al_2O_3 and CaO in the plagioclase-bearing areas while the crystal-free gap glass has a composition similar to that of the starting material.

3.2.3. Equilibrium, Crystal-Bearing Melt Regime

Runs 3 and 4 were stopped once the viscosity was deemed constant (within ±0.05 log Pa s) over a period of at least 10 h. The final apparent viscosity of runs 3 and 4 differs by 0.2 log Pa s. BSE image analysis reveals homogeneously distributed plagioclase and similar crystal alignment with the flow line in each experimental product (Figure 5). The crystal fraction is similar in both experiments (Figure 6), but the crystal density distribution and the average plagioclase maximum length over the analyzed images vary from 42 to 24

Table 5. Results of Subliquidus Viscosity Measurement (η_{app}), Including Phase Proportion (ϕ in %), Aspect Ratio (R) and Nucleation (I_r), and Growth Rate (G_r)

T_{exp} (°C)	1180	1168	1162 run 3	1162 run 4	1157	1152	1144
log η_{app} (Pa s)[a]	3.59	3.77	4.05	3.86	3.93	4.11	4.80
$\dot{\gamma}$ (s^{-1})	0.042	0.042	0.042	0.042	0.042	0.042	0.011
log η_{melt} (Pa s)	3.22	3.37	3.48	3.45	3.56	3.38	3.51
log η_r (Pa s)	0.37	0.40	0.57	0.41	0.37	0.73	1.29
K[b] (Pa s)	4785.5	6220.2	6955.7	6798.4	7447.1	7418.5	12,663
n[b]	0.99	0.98	0.83	0.96	0.91	0.76	0.61
R^2	0.999	0.999	0.998	0.999	0.999	0.999	0.991
K_r (K/η_{melt})	2.88	2.65	2.30	2.41	2.05	3.09	3.91
ϕ_{melt} (%)	92.8	87.7	87.1	87.1	87.3	86.5	82.7
ϕ_{oxide} (%)	0.4	0.9	0.5	0.7	0.5	0.4	0.6
$\phi_{plagioclase}$ (%)	6.8	11.4	12.4	12.2	11.8	12.3	14.5
$\phi_{pyroxen}$ (%)						0.9	2.2
ϕ	0.07	0.12	0.13	0.13	0.12	0.14	0.17
R	6.3	6.5	7.4	8.0	9.1	11.2	11.0
ϕ_{max}	0.40	0.40	0.38	0.37	0.35	0.32	0.32
N_a (mm^{-2})	2.85	29.12	42.25	24.11	24.62	25.58	15.47
G_r (m/s)	7.9E-10	1.0E-09	8.56E-10	1.50E-09	9.5E-10	7.4E-10	3.4E-09
I_r (1/m^3 s)	2.2E+04	1.0E+06	2.0E+06	1.0E+06	8.7E+05	7.0E+05	6.0E+05

[a]Apparent viscosity at t_4 measured at the strain-rate indicated below.
[b]K and n are fitting parameters calculating using equation (3).

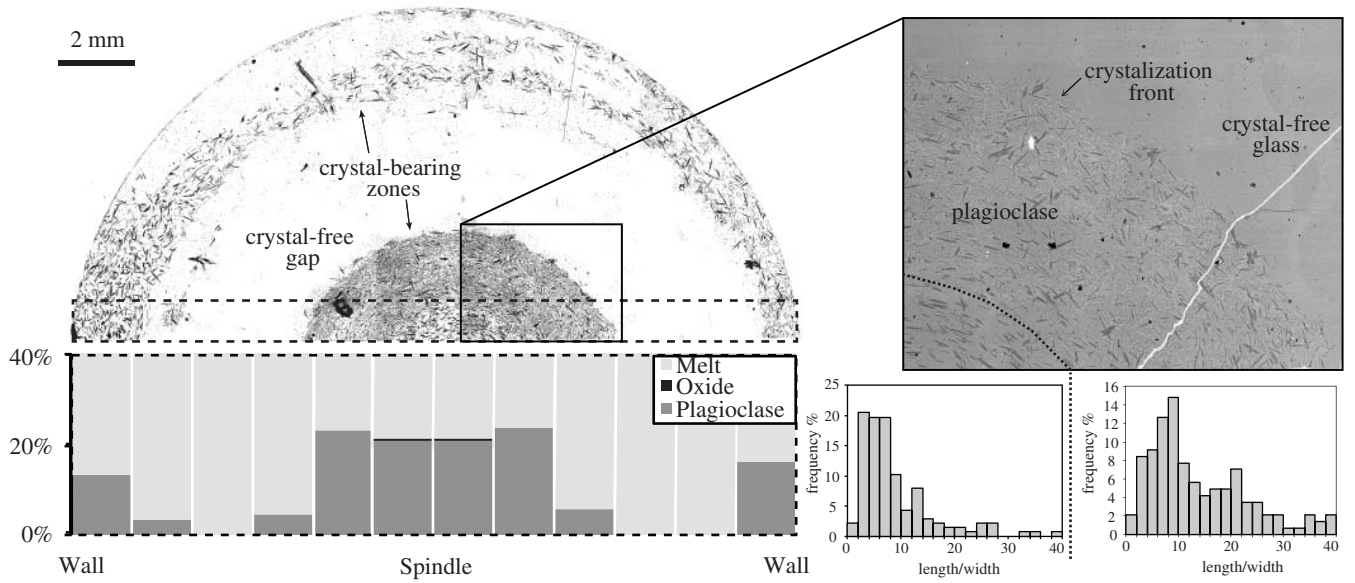

Figure 4. Binary image of the final product quenched during run 2 at 1162°C with the corresponding crystal fraction across the sample (dashed-lined box). The zoomed image is a BSE image showing the crystallization front and two areas within the crystal-bearing zone and corresponding plagioclase aspect-ratio frequency plots.

crystal/mm^2 and 0.66 to 0.99 mm for runs 3 and 4, respectively (Figure 7). This constrains crystal growth rates of 8.6 $\times$ 10^{-10} and 1.5 $\times$ 10^{-9} m/s in runs 3 and 4, respectively.

3.3. Isothermal Experiments: Suspension Viscosity at Subliquidus Temperatures

All recorded viscosity-time measurements at various subliquidus temperatures are displayed in Figure 8 and reported in Table 4 and as well as in Table 5 together with proportion and characteristics of the phases encountered.

The incubation time ($t_2 - t_1$) varies between 7 and 118 h, but exhibits no direct relationship with the T_{exp}. During the incubation time, viscosity increases slightly at a rate of 9.5 $\times$ 10^{-4} log Pa s/h at 1180°C and 2.9 $\times$ 10^{-3} log Pa s/h at 1144°C. The rate of the subsequent viscosity increases due to extensive crystallization from t_2 to t_3 varies from 4.1 $\times$ 10^{-3} log Pa s/h at 1180°C to 2.6 $\times$ 10^{-2} log Pa s/h at 1144°C. Here the rate of viscosity increase is exponential with a reduction in T_{exp} (Figure 9). The end of the sharp viscosity increase (t_3) marks the end of extensive crystallization and the beginning of stage 4—a regime with a more or less constant viscosity.

The strain-rate dependence of the apparent viscosity was investigated at t_4 by imposing different angular velocities. Each change in strain-rate is accompanied by an immediate response of the measured torque, which asymptotically approaches a stable value after a period of a few hours. We observe that an increase in strain-rate decreases the apparent viscosity. This shear-thinning effect appears more pronounced at lower temperatures where the crystallinity is higher (Figure 8b).

The BSE images of the experimental products are shown in Figure 5. The profile of crystal content of the suspension between the spindle and the wall is presented in Figure 6 and the maximum length distribution of the plagioclase in Figure 7. Plagioclase is the dominant crystal phase (Table 5) and is homogeneously distributed throughout all final products, with the exception of the run at 1144°C, in which the crystal fraction is twice as high near the spindle as it is near the wall. Plagioclase first appears along with oxides around 1180°C ($\phi = 0.07$); pyroxene appears below 1152°C. By 1144°C, the crystallinity reaches $\phi = 0.17$; for this last sample the average crystal fraction was taken near the spindle, neglecting the area on the outside near the crucible wall.

The shape of the plagioclase is typically acicular to tabular in cross section, with a minor fraction of hopper habits increasingly common at the lowest temperatures. The average aspect ratio of the plagioclase increases from 6.3 at 1180°C to 11 at 1144°C. The maximum growth rate is on the order of 10^{-9} m/s and

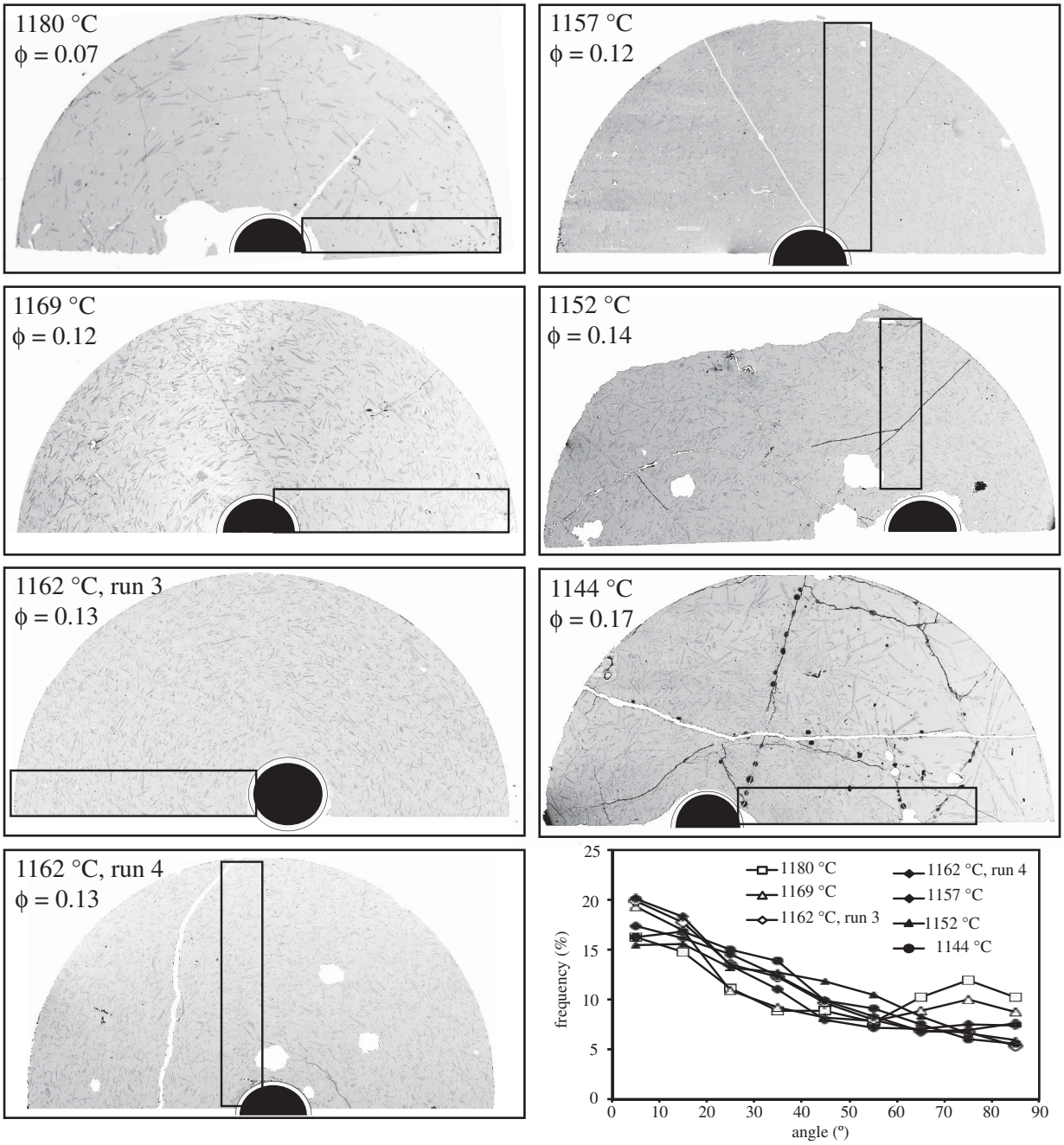

Figure 5. BSE images of final products cut perpendicular to the spindle. The boxes mark the area where crystal fraction profiles were calculated.

nucleation rates vary between 2.2×10^4 and 2×10^6 m^{-3}/s. Pyroxene, which is present at 1152 and 1144°C, exhibits a preferential concentration along the spindle and an absence near the wall. The average aspect ratio of pyroxenes and of oxides is ~1. In the high-temperature experiments ($T_{exp} \geq 1167$°C) individual plagioclase are isolated within the suspending melt whereas at lower temperatures (1162°C $\geq T_{exp} \geq$ 1144°C) and higher crystallinity, the crystals are in contact with each other and physically interact during flow. All cross sections clearly display a preferential alignment of elongated plagioclase subparallel (within 20° or less) to the flow lines around the rotating spindle (Figure 5).

The chemical compositions of the phases are given in supporting information. The chemical composition of the interstitial melt displays a slight fractionation with increasing crystallinity of the suspensions. With the

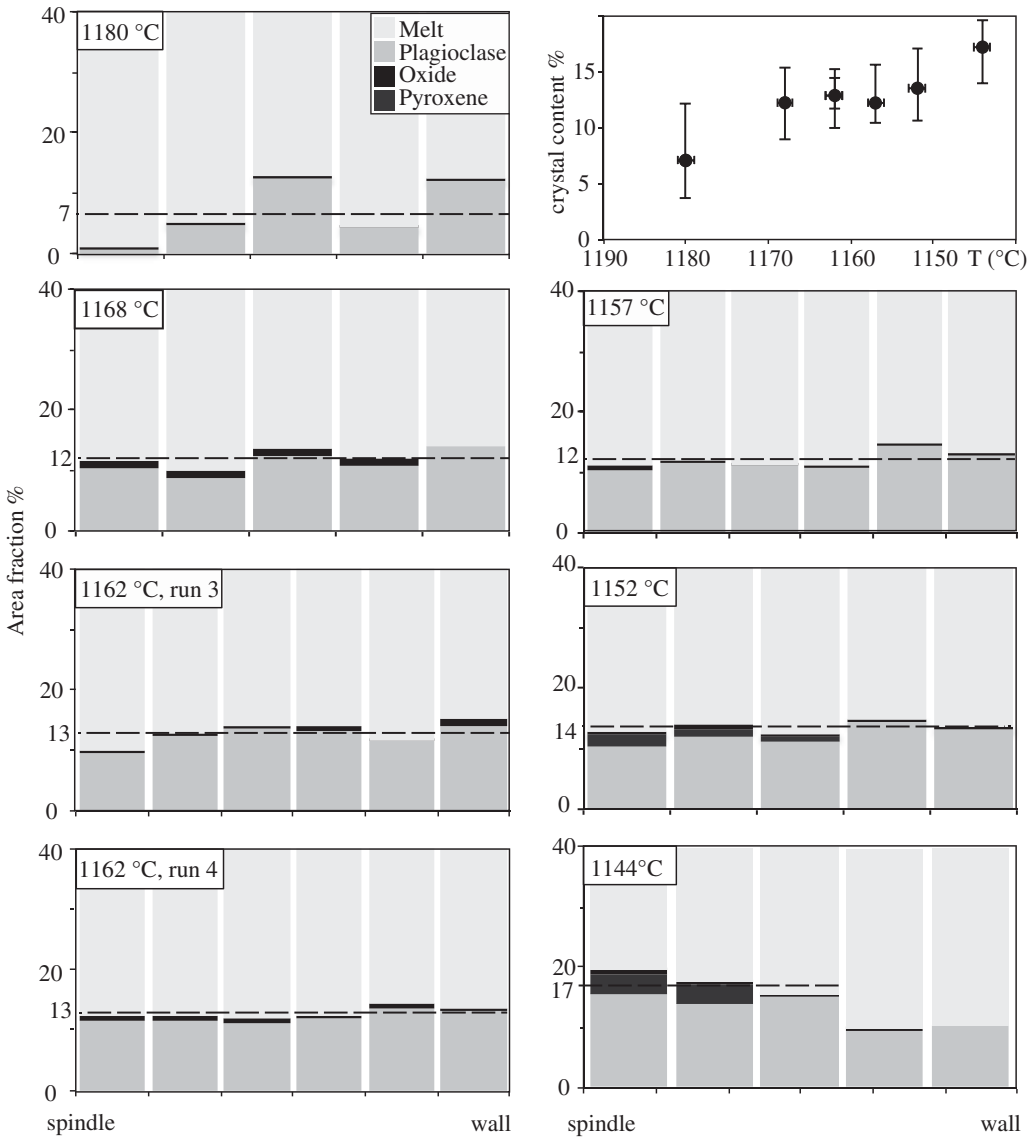

Figure 6. Crystal content (in %) calculated within 2 mm^2 areas (see Figure 5) and displayed as function of experimental temperature (the error bars represent the crystal range calculated for each samples).

initial growth of oxides and plagioclase (1180–1157°C), the interstitial melt composition slightly increases in SiO_2 (up to 60 wt %) and decreases in Al_2O_3, CaO of about 1 wt %. Then, below 1152°C when pyroxenes appear (corresponding to 14% of crystals and 86% of melt) the relative content of SiO_2 decreases whereas Al_2O_3, CaO, and Na_2O remain approximately constant. We also noted that the interstitial melt produced at 1144°C (not shown here) shows strong fluctuations in SiO_2 concentration between the area near the spindle where pyroxenes are homogeneously distributed and the area where only plagioclase crystals are present.

Plagioclase compositions range between An_{72} and An_{79} and no zoning was observed. We observe no obvious change in anorthite content with decreasing temperature and increasing crystallinity. The pyroxenes are enstatites, En_{82} and En_{81} for the suspensions formed at 1152°C and 1144°C, respectively.

4. Discussion

4.1. Incubation Time

The repeated experiment at 1162°C shows that incubation time may vary significantly from one experiment to another. This implies that external factors other than undercooling temperature, cooling rate, and time

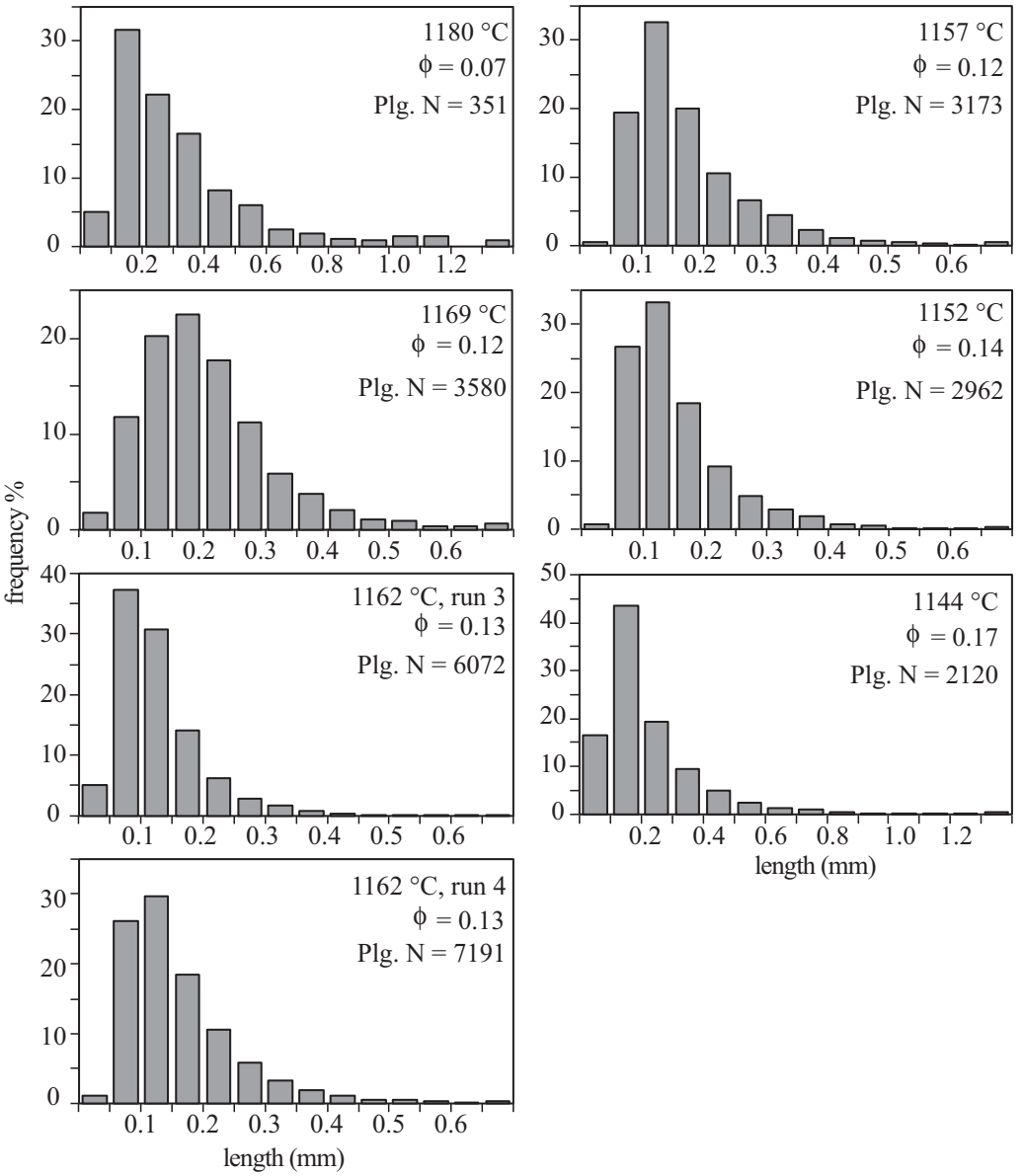

Figure 7. Distribution of the plagioclase long axis length measured within the whole BSE images from Figure 5 for each sample; ϕ represents the crystal fraction and Plg. N the number of measured plagioclase.

above the liquidus (identical for all repeated experiments) are influencing the nucleation and incubation process [*Gibb*, 1974; *Tsuchiyama*, 1983]. One of them is the surface roughness of the spindle and the crucible wall, which reduces the interfacial free energy, favoring heterogeneous nucleation. Cooling preferentially along the spindle and the crucible wall may also enhance localized nucleation. Hence, slight differences between crucibles or the spindles used for the experiments (in particular due to the fact that the three-folded welded tip of the spindle is hand-made), would lead to variation in incubation nucleation time. Another factor is the effects of external vibrations due to other activities in the laboratory. These mechanical motions would facilitate the rearrangement of atoms in the melt shortening the incubation time [*Gibb*, 1974]. We are left with the conclusion that the incubation and onset of crystallization can be stochastic in these multicomponent systems. Such phenomenon has also been observed for crystallization of plagioclase from supercooled basaltic melts by *Gibb* [1974] but interestingly has not been observed for crystallization of olivine [e.g., *Donaldson*, 1979].

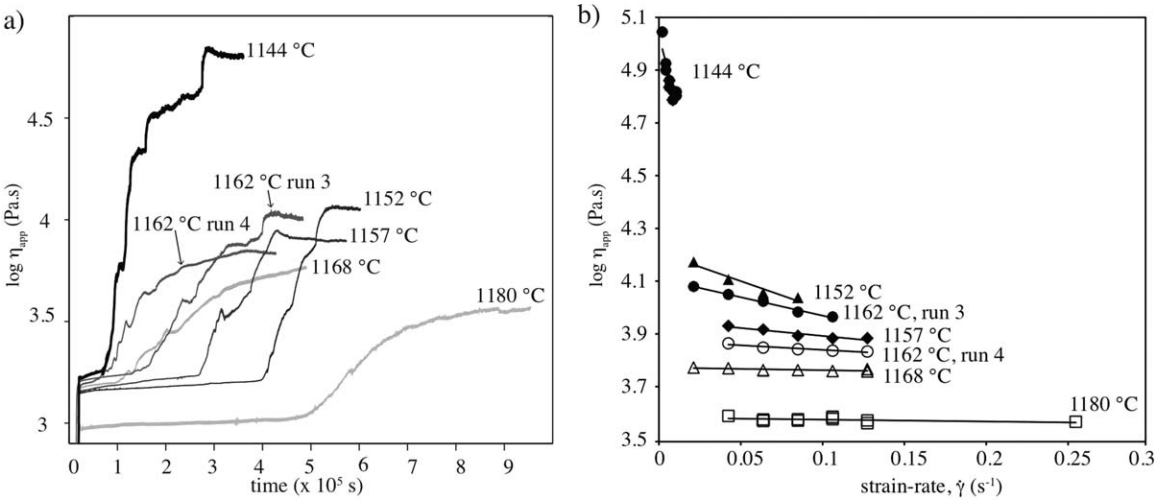

Figure 8. (a) Temporal evolution of viscosity measurements during melt crystallization at different subliquidus temperatures. (b) Variation of the apparent viscosity as a function of strain-rate and subliquidus temperature. Note: The viscosity values were recorded at decreasing strain-rate steps. The viscosity values recorded at subsequent increasing strain-rate steps (not shown here) are systematically 0.02 log unit higher—an hysteresis suggesting a component of strain hardening [see *Cimarelli et al.*, 2011].

The nucleation theory proposed by *Kirkpatrick* [1983] relates the nucleation time to the temperature and activation energy for atomic or molecular attachment and suggests that nucleation should typically be faster for less polymerized melt. The rate of atom attachment depends on the supply of chemical compounds from the melt by diffusion and magma mixing. Therefore, faster stirring of low viscosity depolymerized melt will cause a more effective chemical homogenization, which strongly reduces the incubation nucleation time and decreases the delay of crystallization [*Kouchi et al.*, 1986]. Comparing to the observations for crystallizing basaltic lava samples from Stromboli or Etna [*Vona et al.*, 2011], at similar degree of undercooling the incubation times recorded for our more polymerized andesite are (on average) one order of magnitude longer.

The slight viscosity increases during the incubation time may be related to Fe oxidation and possibly, slight melt fractionation. Under constant oxygen fugacity, the ratio of Fe^{3+} to total iron increases with decreasing temperature. This change in oxidation state may also generate changes in the structural role of iron within the melt [*Mysen et al.*, 1984; *Giuli et al.*, 2003; *Wilke et al.*, 2007] and viscosity has been demonstrated to increase with oxidation of iron [e.g., *Dingwell and Virgo*, 1987; *Dingwell*, 1991; *Bouhifd et al.*, 2004; *Chevrel et al.*, 2013]. According to the model of *Kress and Carmichael* [1991], the redox state of our sample would change from $Fe^{3+}/(Fe^{3+} + Fe^{2+}) = 0.4$ at 1400°C to $Fe^{3+}/(Fe^{3+} + Fe^{2+}) = 0.7$ at 1162°C. Although there is no model to estimate quantitatively the effect of redox state on viscosity, we interpret the trends provided in *Dingwell* [1991] to infer that the oxidation of iron could quantitatively yield the slight viscosity increase during incubation time. Further, chemical analysis of the glass in samples quenched during incubation (run 1 at 1162°C) reveals slight chemical variations in comparison with the

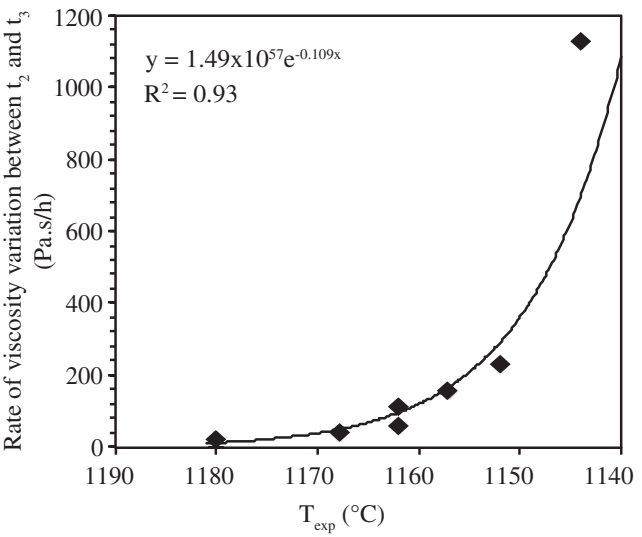

Figure 9. Rate of viscosity variation during extensive crystallization between t_2 and t_3, as a function of the temperature of the experiments.

starting materials, which may be attributed to the onset of fractionation as oxide and plagioclase nucleate. The viscosity difference calculated for this change in chemistry (estimated using the model of *Giordano et al*. [2008]) is also on the order of what is observed.

4.2. Transient Rheological Evolution During Crystals Growth

Figure 9 shows that the rate of viscosity variation between t_2 and t_3, (the stage of extensive crystallization) exponentially increases with ΔT. Although one might be tempted to propose a correlation between the rate of viscosity increase and crystal growth rate, the BSE image analysis of the sample from an experiment stopped in the middle of extensive crystallization (run 2 at 1162°C; Figure 4) reveals that the crystal distribution is heterogeneous, with preferential crystal nucleation prevailing near the spindle and near the wall. The spatially heterogeneous crystal growth generates chemically heterogeneous interstitial melts across the suspension: an unfractionated, crystal-free melt in the sample core, bordered by more evolved residual melt in the interstices of the plagioclase-rich zones near the spindle and the crucible wall. Plagioclase growth is thereby forced to progress into the unfractionated crystal-free gap of the profile due to the chemical gradient and higher availability of chemical compounds. The progression of plagioclase growth is suggested to advance from the spindle to the wall, rather than the opposite, due to the high strain-rate profile near the spindle. As crystal growth ensues, the crystal nucleation front migrates outward toward the undifferentiated melt. The phase transformation (from melt to crystals) can most likely be described by two simultaneous processes: further growth of existing crystals and the propagation of a front of newly formed crystals advancing from the spindle toward the crucible wall (nucleation). A homogeneous distribution of growing crystals was not observed.

The observed viscosity increase is, we propose, caused by this moving crystallization front, an increase in crystal fraction and change in melt composition. These combined processes are not perfectly continuous as some variations in the viscosity increase rate are observed (small arrows in Figure 3). The maximum viscosity at t_3 likely marks the point where the crystallization front reached the crystal-bearing zone near the crucible wall. The subsequent mild viscosity drop and stabilization is likely caused by crystal redistribution and alignment in the flow field.

In the same manner, pyroxene growth is initiated near the spindle, where the strain-rate is the higher, and would migrate outward. The final products of experiments 1152 and 1144°C showing this heterogeneous pyroxene distribution suggest that thermodynamic equilibrium was not reached although the viscosity has became constant through time (due to the rheologically imperceptible effect of such low pyroxene content). For future work, experimentalists should wait longer time in order to ensure a most complete pyroxene distribution.

4.3. Effect of Stirring on Crystallization of Andesite

To our knowledge only one experimental study [*Iezzi et al*., 2011] has focused on the crystallization of andesitic melt at ambient pressure and it was performed under static conditions. Other studies have performed crystallization experiments under confined pressure [e.g., *Hammer and Rutherford*, 2002; *Couch et al*., 2003; *Iezzi et al*., 2008; *Calzolaio et al*., 2010; *Arzilli and Carroll*, 2013] or have focused on crystallization kinetics of basaltic and rhyolitic liquids [e.g., *Swanson*, 1977; *Hammer*, 2004; *Conte et al*., 2006; *Hammer*, 2006; *Pupier et al*., 2007; *Schiavi et al*., 2009; *Mollard et al*., 2012; *Agostini et al*., 2013]. This study is unique in describing the crystallization kinetics of an andesite under ambient pressure and under dynamic (stirring) conditions.

4.3.1. Crystal Shape

Lofgren [1974] performed isothermal experiments and described the strong dependence of plagioclase crystal morphology on undercooling temperature. More recently, *Iezzi et al*. [2011] showed that the shape of plagioclase is influenced by the imposed cooling rate. Although the undercooling temperature changes, the cooling rate is the same in each experiment and the shape of the plagioclase remains similar throughout-acicular to tabular with a variable proportion of hopper habits, with a tendency toward more acicular and hopper shape for the low temperature experiments (1144°C). The near constancy in shape of the crystal is probably due to the narrow range of undercooling temperatures (<40°C), in agreement with *Lofgren* [1974]. As suggested by *Kouchi et al*. [1986] stirring also influences the crystal shape; a constant flow of the liquid phase stabilizes the crystal interface morphology (producing flat faces) and reducing the size of the crystals. With respect to the sample at 1144°C, the large acicular to hopper plagioclase crystals near the crucible wall at the right side of the spindle and their nonalignment with the flow line indicate the lack of flowing, due to the offset of the spindle. The experimental setup being always the same, we suggest that if the

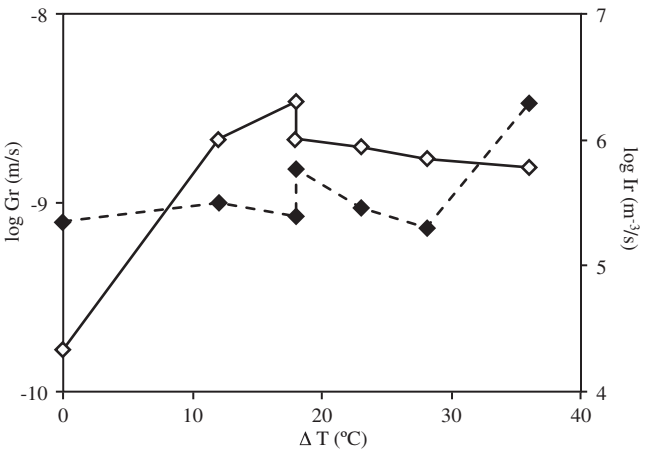

Figure 10. Nucleation rate (I_r) (open symbols) and crystal growth (G_r) (solid symbols) as function of undercooling temperature.

spindle is not centered this is due to fast crystal growth that pushed the spindle, in the flow field, to minimize flow resistance, resulting in more space available for crystals to grow.

Undercooling temperature, cooling rate, and shear stress influence therefore dramatically the plagioclase shape and may have important effects on viscosity.

4.3.2. Plagioclase Nucleation and Growth Rate

It should be noted that since the chemical composition of the residual melt did not dramatically change as crystal content increases (with respect to the starting melt) the undercooling temperature ($\Delta T = T_{liquidus} - T_{exp}$) may, to a first approximation, be considered constant with time during each experiment, and crystallization processes can be discussed as a function of a single undercooling temperature. The lack of chemical zoning in the plagioclase supports this approximation. The influence of undercooling temperature on plagioclase growth and nucleation rate (calculated between t_1 and t_3) under continuous stirring is represented in Figure 10. At $\Delta T = 0$, we observe that the nucleation process was active (not null) and the growth rate was of 10^{-10} m/s producing about 7% of plagioclase. This implies that the liquidus temperature observed here under stirring is higher than that calculated by MELTS, and that stirring reduces the incubation time (in agreement with *Kouchi et al*. [1986]), and favors crystal nucleation and growth even very close to the liquidus.

Theoretically, the growth rate should be higher at low undercooling with respect to high undercooling conditions, where nucleation is favored [e.g., *Fenn*, 1977; *Swanson*, 1977]. However, here we observe that the nucleation does not keep accelerating as a function of ΔT, rather it remains constant above $\Delta T = 20°C$; and the growth rate is nearly constant as ΔT increases (as observed in *Vona and Romano* [2013]) and does not show the typical *bell* shape curve of the growth rate versus ΔT [e.g., *Fenn*, 1977; *Swanson*, 1977; *Orlando et al*., 2008; *Arzilli and Carroll*, 2013]. Although current models cannot explain both behaviors, the stirring may be an important factor. As stirring results in an extensive circulation of the elements, it enhances the probability of the atoms to cluster to form a nucleus and provide a rapid supply of elemental nutrients to the crystals during growth. The stirring of the melt seems to favor nucleation even at lower undercooling and to maintain a nearly constant crystal growth rate. We highlight here that both undercooling and stirring strongly control the crystallization kinetics of silicate melts. We recognize however that the lack of higher undercooling experiments prevents the full description of the behavior of crystal nucleation and growth versus undercooling.

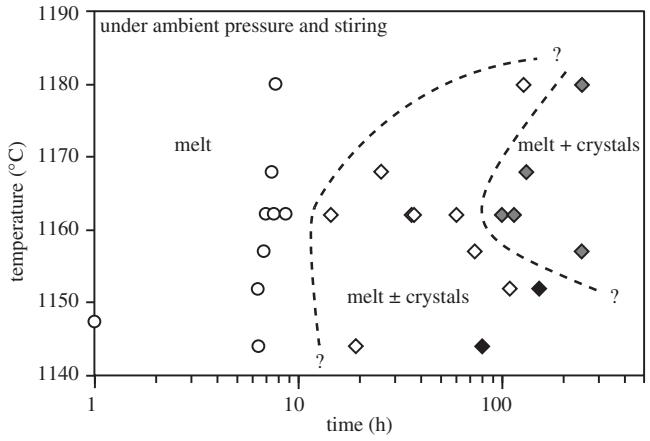

Figure 11. Time-Temperature-Transformation (TTT) diagram built from the kinetic variation of viscosity. Open circles correspond to pure melt phase (at t_1), open and black diamonds correspond to the presence of crystals in some amount but not in equilibrium (oxide ± plagioclase at t_2 and oxide + plagioclase ± pyroxene at t_3, respectively) and gray diamonds correspond to the presence of crystals in constant amount (at t_3).

4.4. Time-Temperature-Transformation Diagram

Using the rheological response of the material to undercooling over time, a TTT (Time-Temperature-Transformation) diagram, commonly used to describe the behavior of nucleation and crystallization, can be constructed (Figure 11). Each temperature and time interval is assigned to a petrographic description: "melt" defines the area where only liquid phase exists; "melt ± crystals" defines the area where crystals are present in some amount but not in equilibrium, this area is delineated somewhere between t_1 and t_2 and until thermodynamic equilibrium is achieved, at t_3, where the "melt + crystals" area starts, representing the area where crystallization content is fixed (thermodynamic equilibrium between crystal and melt) and viscosity becomes constant. We noted that for the lowest temperature experiments (1152 and 1144°C), although viscosity was observed to be constant through time, evidence exists (heterogeneous pyroxene distribution) that thermodynamic equilibrium may not have been achieved. We observe that the time needed for crystals to form decreases with increasing undercooling temperature, in agreement with classical nucleation theory and previously reported experimentally [e.g., *Tsuchiyama*, 1983; *Kouchi et al*., 1986] and that it may increase at lower temperature.

This TTT diagram represents the crystallization nose for an andesite under isothermal stirring conditions and at ambient pressure. The diagram also suggests that the liquidus temperature must be above 1180°C. Estimating the temperature or the time required to form crystals and thus change of the rheology of the lava now becomes possible.

4.5. Rheological Effect of the Crystal Cargo

The relative viscosity, that is the difference between the measured apparent viscosity and the calculated interstitial melt viscosity, is presented as a function of the crystal fraction and compared with previous similar studies in Figure 12. It is observed that our results have a higher relative viscosity for a given particles content than previous studies and than the models proposed by *Costa et al*. [2009] (using the fit parameters from *Cimarelli et al*. [2011]) and by *Ishibashi* [2009]. The difference with the models may be due to the high aspect ratio of the crystallizing plagioclase that is in average higher than what was measured in previous studies (e.g., analog studies: $R = 9$ for *Cimarelli et al*. [2011]; 9.17 for *Mueller et al*. [2010] and natural material studies 7.2 for *Vona et al*. [2011]; 4.9 for *Ishibashi and Sato* [2007]). However, for a more thorough comparison with analogue and analytical models, the viscosity of samples with higher crystal content should be measured, which is impossible with the apparatus used in this study.

As shown by Figure 8b, the suspensions exhibit shear-thinning behavior (see also the discussion in *Ryerson et al*. [1988] and *Ishibashi and Sato* [2007]). In our experiment, the onset of non-Newtonian behavior,

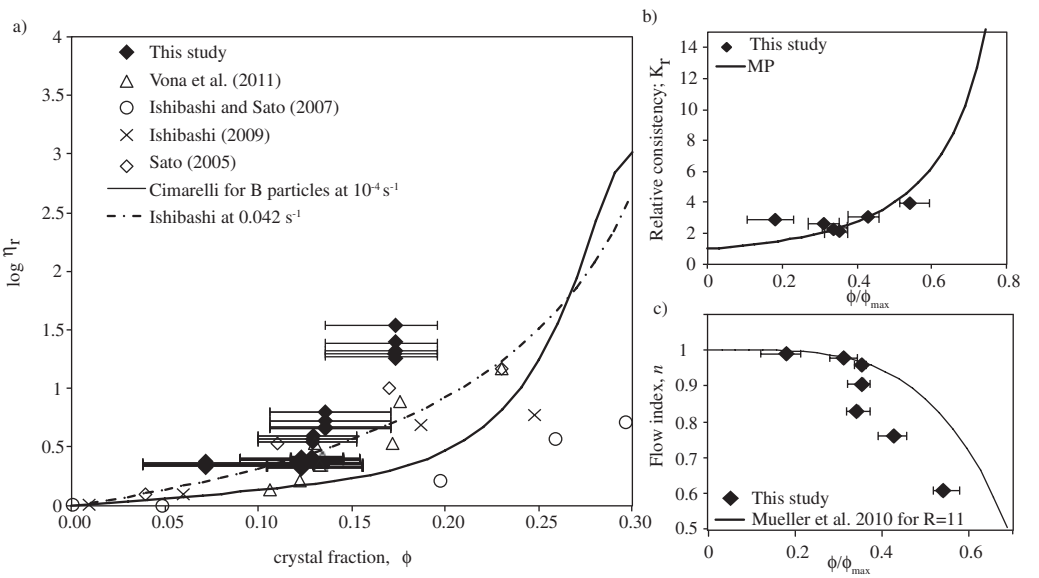

Figure 12. (a) Relative viscosity as function of crystal fraction. Horizontal error bars represent the range of crystallinity measured across the sample. (b) Relative consistency as a function of the normalized crystal fraction by the maximum packing. Black line refers to the Maron-Pierce relation: $K_r = \eta_{melt}(1 - \phi/\phi_{max})^2$. (c) Flow index, n, as a function of the normalized crystal fraction by the maximum packing. Black line refers to the relationship given by *Mueller et al*. [2010] for particles aspect ratio of $R = 11$.

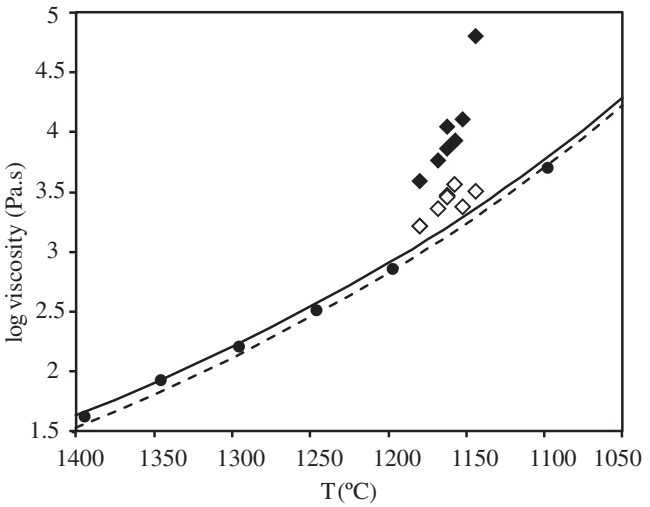

Figure 13. Viscosity-temperature relationship. Black circles are the viscosity measurements for the melt after 1 h of thermal equilibrium. Black diamonds are the viscosity measured at isoviscous conditions at the end of the experiments at 0.2 RPM (0.042 s^{-1}) except the lowest temperature (1144°C) that was taken at 0.05 RPM (0.011 s^{-1}), as given in Table 5. White diamonds are the viscosity of the interstitial melt calculated using *Giordano et al*. [2008]. The black line is the viscosity-temperature relationship experimentally determined and the dashed line is the viscosity-temperature relationship calculated using *Giordano et al*. [2008] from the bulk rock composition.

represented by the deviation from $n = 1$ (Figure 12c) is noted at crystal fractions as low as 0.13 ($\phi/\phi_{max} = 0.3$ and $T < 1162$°C). This particle fraction is considerably lower than the usually suggested boundary of $\phi = 0.25$–0.30 [*Shaw*, 1969; *Pinkerton and Stevenson*, 1992; *Lejeune and Richet*, 1995; *Petford*, 2009; *Costa*, 2005; *Costa et al*., 2009] but in agreement with previous experiments performed with a concentric cylinder on natural magmas [i.e., *Ishibashi and Sato*, 2007; *Vona et al*., 2011; *Ishibashi*, 2009; *Sehlke et al*., 2014] and with the description of suspensions containing acicular particles [e.g., *Mueller et al*., 2010; *Cimarelli et al*., 2011; *Moitra and Gonnermann*, 2015]. The likely cause is that high-aspect-ratio crystals, in our case plagioclase ($6 < R < 11$), commonly interact even at low crystal fraction (e.g., experiments at $T_{exp} < 1162$°C). Furthermore, suspensions with a wider particle size distribution are also estimated to start to interact at lower crystal fractions than homogeneous suspensions. At 1144°C, the flow index, n, was calculated to be as low as 0.6, that is significantly lower than what is predicted for aspect ratio of $R = 11$ using the model by *Mueller et al*. [2010]. This strong strain-rate dependence is likely due to alignment with the flow lines. At high strain-rate, the particles are pulled and forced to align with the flow lines and hence a relatively lower viscosity is recorded; this effect is enhanced with an increase in crystallinity. At low strain rates, the particles are not fully aligned within the flow, promoting interaction, with the net effect of increasing the relative viscosity.

We report the rheological map of the Tungurahua andesite as a function of the temperature for atmospheric conditions (Figure 13). The liquid viscosity measurements show very good agreement with the empirical model of *Giordano et al*. [2008] that was therefore used to estimate the interstitial melt viscosity from its composition. The highest apparent viscosity, reached at the limitation of the apparatus, was obtained for the sample equilibrated at 1144°C corresponding to 17% of crystals and a viscosity of 5.4 log Pa s for a strain-rate of 0.002 s^{-1}. Lower temperature and higher crystallinity could not be obtained for such composition with this experimental setup. In order to complete this rheological map toward lower temperature and higher crystallinity another experimental setup must be devised.

5. Conclusion

Viscosity measurements of crystallizing andesitic lava from Tungurahua volcano were performed in air at subliquidus temperatures using the concentric cylinder setup. A new disposable spindle made of alumina and sheathed with platinum to avoid contamination was left in the suspension through quenching to preserve the crystallization and flow textures obtained for a range of temperature and time conditions. Temporal experiments were conducted at the subliquidus temperature of 1162°C to test the crystallization kinetics and associated suspension viscosity. The experiments show that crystals nucleate near the spindle and crucible wall and a crystallization front is observed to move inward. Upon stirring, the crystals align with the flow lines. The rheological response obtained in these dynamic tests is not simply related to crystal fraction alone, but to the interplay between crystal nucleation, crystallization front migration, and crystal growth (and resultant melt chemistry fractionation), interaction and alignment within the flow lines.

Isothermal experiments were then performed to test the suspension viscosity at subliquidus temperatures. Textural analyses suggest that nucleation initiates with plagioclase and oxides at 1180°C and pyroxenes appear at 1152°C. By 1144°C, 17% crystals are present in the suspension. The nucleation rate is around 2.2 $\times 10^4$ to 2 $\times 10^6$ m^{-3}/s and the maximum growth rate of plagioclase is calculated to be on the order of 10^{-9} m/s. Crystallization kinetics (including nucleation and growth rate) seem to be influenced by the continuous stirring of the experiments that favor vigorous atomic circulation within the sample. A unique TTT diagram was built using the kinetic viscosity variations and petrographic observations, representing the crystallization nose for an andesite under stirring conditions and at ambient pressure. The cooling path, the undercooling temperature, and the deformation history of an andesitic liquid controls the crystallization kinetics and the crystal shapes, implying important effects on viscosity. Understanding how the rheology of magma evolves while deforming and cooling is potentially of great interest to modeling conduit processes, effusive behavior and thus hazard reduction.

The effect of the crystal cargo on the viscosity at stable crystal content and distribution is measured to be higher than expected and the onset of non-Newtonian, shear-thinning, behavior is evidenced at crystal content as low as 13%. The discrepancies with common models are likely due to the more acicular shape of naturally growing plagioclase, the wider scatter in crystal dimensions and the more complex physicochemical interactions between the evolving residual melt and growing crystals than the suspensions used to generate the current, state of the art models. The contrasting dynamic rheology observed here highlights the needs for further rheological investigations of intermediate lava crystallization.

Acknowledgments

M.O. Chevrel wishes to thank THESIS (Elitenetzwerk Bayern) for financial support. C. Cimarelli acknowledges Marie Curie funding (BEACon, 235328) from the European Commission and funds from AXA Research Fund. Y. Lavallée acknowledges funding from the European Research Council (ERC) Starting Grant on Strain Localisation in Magmas (SLiM, 306488) as well as the Deutsche Forschungsgemeinschaft (DFG) grants LA2651/1-1 and LA2651/3-1. D.B. Dingwell acknowledges support from the European Research Council (ERC) Advanced Grant on Explosive Volcanism in the Earth System (EVOKES, 247076). This investigation was conducted at the University of Munich (LMU), and all the data can be requested from the corresponding author. We thank Kelly Russell and an anonymous reviewer for their constructive comments, which led to significant improvements in this paper.

References

Agostini, C., A. Fortunati, F. Arzilli, P. Landi, and M. R. Carroll (2013), Kinetics of crystal evolution as a probe to magmatism at Stromboli (Aeolian Archipelago, Italy), *Geochim. Cosmochim. Acta*, *110*, 135–151.

Arzilli, F., and M. R. Carroll (2013), Crystallization kinetics of alkali feldspars in cooling and decompression-induced crystallization experiments in trachytic melt, *Contrib. Mineral. Petrol.*, *166*, 1011–1027.

Avard, G., and A. Whittington (2012), Rheology of arc dacite lavas: Experimental determination at low strain rates, *Bull. Volcanol.*, *74*, 1039–1056.

Bagdassarov, N., and D. B. Dingwell (1992), A rheological investigation of vesicular rhyolite, *J. Volcanol. Geotherm. Res.*, *50*, 307–322.

Bagdassarov, N. S., D. B. Dingwell, and S. L. Webb (1994), Viscoelasticity of crystal-bearing and bubble-bearing rhyolite melts, *Phys. Earth Planet. Inter.*, *83*, 83–99.

Bouhifd, A., P. Richet, P. Besson, M. Roskosz, and J. Ingrin (2004), Redox state, microstructure and viscosity of a partially crystallized basalt melt, *Earth Planet. Sci. Lett.*, *218*, 31–44.

Calzolaio, M., F. Arzilli, and M. R. Carroll (2010), Growth rate of alkali feldspars in decompression-induced crystallization experiments in a trachytic melt of the Phlegraean Fields (Napoli, Italy), *Eur. J. Mineral.*, *22*, 485–493.

Caricchi, L., L. Burlini, P. Ulmer, T. Gerya, M. Vassalli, and P. Papale (2007), Non-Newtonian rheology of crystal-bearing magmas and implications for magma ascent dynamics, *Earth Planet. Sci. Lett.*, *264*, 402–419.

Castruccio, A., A. C. Rust, and R. S. J. Sparks (2010), Rheology and flow of crystal-bearing lavas: Insights from analogue gravity currents, *Earth Planet. Sci. Lett.*, *297*, 471–480.

Chevrel, M. O., D. Giordano, M. Potuzak, P. Courtial, and D. B. Dingwel (2013), Physical properties of $CaAl_2Si_2O_8$-$CaMgSi_2O_6$-FeO-Fe_2O_3 melts: Analogues for extra-terrestrial basalt, *Chem. Geol.*, *346*, 95–105.

Cimarelli, C., A. Costa, S. Mueller and H. M. Mader (2011), Rheology of magmas with bimodal crystal size and shape distributions: Insights from analog experiments, *Geochem. Geophys. Geosyst.*, *12*, Q07024, doi:10.1029/2011GC003606.

Conte, A., C. Perinelli, and R. Trigila (2006), Cooling kinetics experiments on different Stromboli lavas: Effects on crystal morphologies and phases composition, *J. Volcanol. Geotherm. Res.*, *155*, 179–200.

Cordonnier, B., K.-U. Hess, Y. Lavallée, and D. B. Dingwell (2009), Rheological properties of dome lavas: Case study of Unzen volcano, *Earth Planet. Sci. Lett.*, *279*, 263–272.

Costa, A. (2005), Viscosity of high crystal content melts: Dependence on solid fraction, *Geophys. Res. Lett.*, *32*, L22308, doi:10.1029/2005GL024303.

Costa, A., L. Caricchi and N. Bagdassarov (2009), A model for the rheology of particle-bearing suspensions and partially molten rocks, *Geochem. Geophys. Geosyst.*, *10*, Q03010, doi:10.1029/2008GC002138.

Couch, S., R. S. J. Sparks, and M. R. Carroll (2003), The kinetics of degassing-induced crystallization at Soufriere Hills Volcano, Montserrat, *J. Petrol.*, *44*, 1477–1502.

Del Gaudio, P., G. Ventura, and J. Taddeucci (2013), The effect of particle size on the rheology of liquid-solid mixtures with application to lava flows: Results from analogue experiments, *Geochem. Geophys. Geosyst.*, *14*, 2661–2669, doi:10.1002/ggge.20172.

Dingwell, D. B. (1986), Viscosity-temperature relationships in the system $Na_2Si_2O_5$-$Na_4Al_2O_5$, *Geochim. Cosmochim. Acta*, *50*, 1261–1265.

Dingwell, D. B. (1991), Redox viscometry of some Fe-bearing silicate melts, *Am. Mineral.*, *76*, 1560–1562.

Dingwell, D. B., and D. Virgo (1987), The effect of oxidation state on the viscosity of melts in the system Na_2O-FeO-Fe_2O_3-SiO_2, *Geochim. Cosmochim. Acta*, *51*, 195–205.

Dingwell, D. B., and S. L. Webb (1989), Structural relaxations in silicate melts and non-Newtonian melt rheology in geologic process, *Phys. Chem. Miner.*, *16*, 508–516.

Donaldson, C. H. (1979), An experimental investigation of the delay in the nucleation of olivine in mafic magmas, *Contrib. Mineral. Petrol.*, *69*, 21–32.

Douillet, G. A., et al. (2013), Sedimentology and geomorphology of the deposits from the August 2006 pyroclastic density currents at Tungurahua volcano, *Bull. Volcanol.*, *75*, 765, Ecuador.

Fenn, P. M. (1977), The nucleation and growth of alkali feldspars from hydrous melts, *Can. Mineral.*, *15*, 135–161.
Ghiorso, M. S., and O. Sack (1995), Chemical mass transfer in magmatic processes. IV: A revised and internally consistent thermodynamic model for the interpolation and extrapolation of liquid-solid equilibria in magmatic systems at elevated temperatures and pressures, *Contrib. Mineral. Petrol.*, *119*, 197–212.
Gibb, F. G. F. (1974), Supercooling and the crystallization of plagioclase from a basaltic magma, *Mineral. Mag.*, *39*, 641–653.
Giordano, D., J. K. Russell, and D. B. Dingwell (2008), Viscosity of magmatic liquids: A model, *Earth Planet. Sci. Lett.*, *271*, 123–134.
Giuli, G., E. Paris, G. Pratesi, C. Koeberl, and C. Cipriani (2003), Iron oxidation state in the Fe-rich layer and silica matrix of Libyan desert glass: A high-resolution XANES study, *Meteorit. Planet. Sci.*, *38*(8), 1181–1186.
Hammer, J. E. (2004), Crystal nucleation in hydrous rhyolite: Experimental data applied to classical theory, *Am. Mineral.*, *89*, 1673–1679.
Hammer, J. E. (2006), Influence of fO_2 and cooling rate on the kinetics and energetics of Fe-rich basalt crystallization, *Earth Planet. Sci. Lett.*, *248*, 618–637.
Hammer, J. E., and M. J. Rutherford (2002), An experimental study of the kinetics of decompression-induced crystallization in silicic melt, *J. Geophys. Res.*, *107*(B1), 2021, doi:10.1029/2001JB000281.
Harris, A. J. L., and J. S. Allen (2008), One-, two- and three-phase viscosity treatments for basaltic lava flows, *J. Geophys. Res.*, *113*, B09212, doi:10.1029/2007JB005035.
Herschel, W. H., and R. Bulkley (1926), Konsistenzmessungen von Gummi-Benzollösungen, *Colloid Polym. Sci.*, *39*, 291–300.
Hui, H., and Y. Zhang (2007), Toward a general viscosity equation for natural anhydrous and hydrous silicate melts, *Geochim. Cosmochim. Acta*, *71*, 403–416.
Iezzi, G., S. Mollo, G. Ventura, A. Cavallo, and C. Romano (2008), Experimental solidification of anhydrous latitic and trachytic melts at different cooling rates: The role of nucleation kinetics, *Chem. Geol.*, *253*, 91–101.
Iezzi, G., S. Mollo, G. Torresi, G. Ventura, A. Cavallo, and P. Scarlato (2011), Experimental solidification of an andesitic melt by cooling, *Chem. Geol.*, *283*, 261–273.
Ishibashi, H. (2009), Non-Newtonian behavior of plagioclase-bearing basaltic magma: Subliquidus viscosity measurement of the 1707 basalt of Fuji volcano, Japan, *J. Volcanol. Geotherm. Res.*, *181*, 78–88.
Ishibashi, H. and H. Sato (2007), Viscosity measurements of subliquidus magmas: Alkali olivine basalt from the Higashi-Matsuura district, Southwest Japan, *J. Volcanol. Geotherm. Res.*, *160*, 223–238.
Kirkpatrick, R. J. (1983), Theory of nucleation in silicate melts, *Am. Mineral.*, *68*, 66–77.
Kouchi, A., A. Tsuchiyama and I. Sunagawa (1986), Effect of stirring on crystallization kinetics of basalt: Texture and element partitioning, *Contrib. Mineral. Petrol.*, *9*, 429–438.
Kress, V. C., and I. S. E. Carmichael (1991), The compressibility of silicate liquids containing Fe_2O_3 and the effect of composition, temperature: Oxygen fugacity and pressure on their redox states, *Contrib. Mineral. Petrol.*, *108*, 82–92.
Landau, L. D., and E. M. Lifshitz (1987), *Fluid Mechanics*, vol. 6, pp. 55–56, Pergamon, Oxford, U. K.
Lavallée, Y., K.-U. Hess, B. Cordonnier, and D. B. Dingwell (2007), Non-Newtonian rheological law for highly crystalline dome lavas, *Geology*, *35*, 843–846.
Lavallée, Y., N. R. Varley, M. A. Alatorre-Ibargüengoitia, K.-U. Hess, U. Kueppers, S. Mueller, D. Richard, B. Scheu, O. Spieler, and D. B. Dingwell (2012), Magmatic architecture of dome-building eruptions at Volcán de Colima, Mexico, *Bull. Volcanol.*, *74*, 249–260.
Lejeune, A.-M., and P. Richet (1995), Rheology of crystal-bearing silicate melts: An experimental study at high viscosities, *J. Geophys. Res.*, *100*, 4215–4230.
Lejeune, A. M., Y. Bottinga, T. W. Trull, and P. Richet (1999), Rheology of bubble-bearing magmas, *Earth Planet. Sci. Lett.*, *166*, 71–84.
Lofgren, G. E. (1974), An experimental study of plagioclase crystal morphology: isothermal crystallisation, *Amer. J. Sci.*, *274*, 243–273.
Mader, H. M., E. W. Llewellin, and S. P. Mueller (2013), The rheology of two-phase magmas: A review and analysis, *J. Volcanol. Geotherm. Res.*, *257*, 135–158.
Manga, M., J. Castro, K. V. Cashman, and M. Loewenberg (1998), Rheology of bubble-bearing magmas, *J. Volcanol. Geotherm. Res.*, *87*, 15–28.
Moitra, P., and H. M. Gonnermann (2015), Effects of crystal shape- and size-modality on magma rheology, *Geochem. Geophys. Geosyst.*, *16*, 1–26, doi:10.1002/2014GC005554.
Mollard, E., C. Martell, and J. L. Bourdier (2012), Decompression-induced crystallization in hydrated silica-rich melts: Empirical models of experimental plagioclase nucleation and growth kinetics, *J. Petrol.*, *53*(8), 1743–1766.
Mueller, S., E. W. Llewellin, and H. M. Mader (2010), The rheology of suspensions of solid particles, *Philos. Trans. R. Soc. A*, *466*, 1201–1228.
Mysen, B. O., D. Virgo, and F. A. Seifert (1984), Redox equilibria of iron in alkaline earth silicate melts: Relationships between melt structure, oxygen fugacity, temperature and properties of iron-bearing silicate liquids, *Am. Mineral.*, *69*, 834–847.
Orlando, A., M. D'orazio, P. Armenti, and D. Borrini (2008), Experimental determination of plagioclase and clinopyroxene crystal growth rates in an anhydrous trachybasalt from Mt Etna (Italy), *Eur. J. Mineral.*, *20*, 653–664.
Petford, N. (2009), Which effective viscosity?, *Mineral. Mag.*, *73*, 167–191.
Pinkerton, H., and G. Norton (1995), Rheological properties of basaltic lavas at sub-liquidus temperatures: Laboratory and field measurements on lavas from Mount Etna, *J. Volcanol. Geotherm. Res.*, *68*, 307–323.
Pinkerton, H., and R. J. Stevenson (1992), Methods of determining the rheological properties of magmas at sub-liquidus temperatures, *J. Volcanol. Geotherm. Res.*, *53*, 47–66.
Pistone, M., L. Caricchi, P. Ulmer, L. Burlini, P. Ardia, E. Reusser, F. Marone, and L. Arbaret (2012), Deformation experiments of bubble- and crystal-bearing magmas: Rheological and microstructural analysis, *J. Geophys. Res.*, *117*, B05208, doi:10.1029/2011JB008986.
Pupier, E., S. Duchene, and M. J. Toplis (2007), Experimental quantification of plagioclase crystal size distribution during cooling of a basaltic liquid, *Contrib. Mineral. Petrol.*, *155*, 555–570.
Ryerson, F. J., H. C. Weed, and A. J. Piwinskii (1988), Rheology of subliquidus magmas. I: Picritic compositions, *J. Geophys. Res.*, *93*, 3421–3436.
Saar, M. O., and M. Manga (1999), Permeability-porosity relationship in vesicular basalts, *Geophys. Res. Lett.*, *26*, 111–114.
Saar, M. O., M. Manga, K. V. Cashman, and S. Fremouw (2001), Numerical models of the onset of yield strength in crystal-melt suspensions, *Earth Planet. Sci. Lett.*, *187*, 367–379.
Sato, H. (2005), Viscosity measurement of subliquidus magmas: 1707 basalt of Fuji volcano, *J. Mineral. Petrol. Sci.*, *100*, 133–142.
Schiavi, F., N. Walte, and H. Keppler (2009), First in situ observation of crystallization processes in a basaltic-andesitic melt with the moissanite cell, *Geology*, *37*, 963–966.
Sehlke, A., A. Whittington, B. Robert, A. Harris, L. Gurioli, and E. Médard (2014), Pahoehoe to 'a'a transition of Hawaiian lavas: An experimental study, *Bull. Volcanol.*, *76*, 876.
Shaw, H. R. (1969), Rheology of basalt in the melting range, *J. Petrol.*, *10*, 510–535.

Stein, D. J., and F. J. Spera (1992), Rheology and microstructure of magmatic emulsions: Theory and experiments, *J. Volcanol. Geotherm. Res.*, *49*, 157–174.

Stein, D. J., and F. J. Spera (2002), Shear viscosity of rhyolite-vapor emulsions at magmatic temperatures by concentric cylinder rheometry, *J. Volcanol. Geotherm. Res.*, *113*, 243–258.

Swanson, S. E. (1977), Relation of nucleation and crystal-growth rate to the development of granitic textures, *Am. Mineral.*, *62*, 966–978.

Tsuchiyama, A. (1983), Crystallization kinetics in the system $CaMgSi_2O_6$-$CaAl_2Si_2O_6$: The delay in nucleation of diopside and anorthite, *Am. Mineral.*, *68*, 687–698.

Villeneuve, N., D. Neuville, P. Boivin, P. Bachèlery, and P. Richet (2008), Magma crystallization and viscosity: A study of molten basalts from the Piton de la Fournaise volcano (La Réunion island), *Chem. Geol.*, *256*, 242–251.

Vona, A., and C. Romano (2013), The effects of undercooling and deformation rates on the crystallization kinetics of Stromboli and Etna basalts, *Contrib. Mineral. Petrol.*, *166*, 491–509.

Vona, A., C. Romano, D. B. Dingwell, and D. Giordano (2011), The rheology of crystal-bearing basaltic magmas from Stromboli and Etna, *Geochim. Cosmochim. Acta*, *75*(11), 3214–3236.

Webb, S., and D. B. Dingwell (1990), Non-Newtonian rheology of igneous melts at high stresses and strain rates: Experimental results for rhyolite, andesite, basalt and nephelinite, *J. Geophys. Res.*, *95*, 15,695–15,701.

Wilke, M., F. Farges, G. M. Partzsch, C. Schmidt, and H. Behrens (2007), Speciation of F in silicate glasses and melts by in-situ XANES spectroscopy, *Am. Mineral.*, *92*, 44–56.